scientific reports

Check for updates

OPEN

Chemical origins of β-Ti stabilization via B_4C additions in metastable β-Ti alloys and composites

Vitor V. Rielli[1]✉, Rodrigo J. Contieri[2] & Sophie Primig[1]✉

The aerospace industry relies on Ti alloys owing to their strength-to-weight ratio and corrosion resistance. In metastable β-Ti alloys, slow cooling from the β-transus leads to partial transformation into coarse α laths, which is detrimental to the mechanical properties. A refinement and decrease of α laths has been previously achieved in β-Ti alloys with B_4C additions. In these materials, the ductility of β-Ti is preserved, and the TiB and TiC particles promote strengthening. However, the mechanism of the β-Ti stabilization remains unclear. Using atom probe tomography, we propose that Mo enrichment in the α-phase limits its growth by reducing the influx of Al from the β-phase. The complex chemical environment near eutectic TiB is enriched in Al and TiO, promoting heterogeneous nucleation of fine α-phase. Increased TiO concentration is observed with the introduction of B_4C. A fundamental understanding of the α-refinement mechanism in Ti-alloys is critical for aerospace applications demanding high performance and reliability.

Keywords Titanium, Beta 21S, TiB, A refinement, Atom probe

Ti alloys are essential for aerospace applications due to their high specific strength, corrosion resistance, and thermal stability[1]. Increasing demands for ductile and yet strong materials for next-generation aircraft engines are often met via microstructure control of Ti alloys via casting and thermo-mechanical processing[2]. The high ductility of the body-centred cubic β-phase makes β-Ti alloys combined with reinforcement particles an attractive choice. These might include carbides (TiC), borides (TiB), and the hexagonally close-packed α-phase[3]. The metastable nature of β-phase often results in a β→α phase transformation during typical air or furnace cooling in industrial applications[4,5]. Faster cooling rates retain the β-phase but are generally avoided as they are known to introduce undesirable residual stress and/or promote the formation of the athermal ω-phase[6,7]. A common strategy to control α-phase formation during slow cooling is to add β stabilizing elements. TiB and TiC have also been shown to be suitable for control of the β→α transformation, in addition to increasing hardness and yield strength properties[8,9].

Beta 21 S is a metastable β-Ti alloy used in the plug-and-nozzle segment of aircraft engines[5]. When reinforced with TiB and TiC and used as a metal matrix composite, it has been demonstrated to deliver more attractive combinations of mechanical properties than the base alloy. A compressive yield strength of 1200 MPa and ductility of > 20% were achieved with a combined volume fraction of 20% of TiB and TiC as discontinuous reinforcements by some of the current authors[10,11]. The most surprising observation was the concomitant decrease and refinement of α, i.e., β stabilization with increasing volume fraction of reinforcement particles. It was hypothesized that the consumption of Ti by these particles led to lower Ti availability in the matrix and a subsequent increase in the β-phase stability. Al, an α-stabilizing element, was thought to be rejected by the growing TiB, which caused them to act as heterogeneous nucleation sites for fine α-phase, as has also been observed for other β-Ti alloys and in Ti-6Al-4 V[12,13]. These hypotheses, however, were only verified indirectly, i.e., via the crystallographic orientation relationship between the individual phases. An advanced understanding of the unknown complex local chemical environment in these microstructures and the fundamental mechanism needs to be established before this can be systematically harnessed. Here, we provide an in-depth analysis of the chemical environment across various interphase boundaries in Beta 21 S with additions of B_4C. Using atom probe tomography (APT), we reveal the mechanism of β stabilization following the formation of reinforcement

[1]School of Materials Science & Engineering, UNSW Sydney, Kensington, NSW 2052, Australia. [2]School of Applied Sciences, University of Campinas-UNICAMP, Limeira 13484-350, SP, Brazil. ✉email: v.vieirarielli@unsw.edu.au; s.primig@unsw.edu.au

particles, where we focus on TiB, the primary reinforcement phase. A better understanding of these phase transformations in β-Ti matrix composites will enable their applications in critical segments of next-generation aircraft. Their high specific strength is important to enable lighter aeroengines, leading to increased fuel efficiency.

Materials and methods

70 g ingots of the Beta 21 S Ti-alloy (Ti-15Mo-3Nb-3Al-0.2Si, wt%) were manufactured in a vacuum arc remelting furnace. B_4C was added at 0.5, 1.5 and 3 wt%. All samples were heat treated in Ar atmosphere at 1000 °C for 12 h, then furnace-cooled (~3 °C/min) to room temperature. The chosen temperature is above the β-transus (~815 °C for Beta 21 S[14]), and the duration was selected to evaluate the microstructure stability at high-temperature exposure, as discussed in[10]. Industrial heat treatments are usually shorter, however, the phenomena discussed here are expected to be equally applicable. In the following, samples are referred to as B_4C_0, B_4C_0.5, B_4C_1.5, and B_4C_3, indicating the corresponding B_4C additions (0, 0.5, 1.5, and 3 wt%). For scanning electron microscopy, samples were polished following standard metallography procedures[15]. Backscatter electron imaging (BSE) was performed in a JEOL 7001 F microscope at 20 kV. The area fraction of α-phase was obtained from an area of 500 μm^2 from BSE images via ImageJ software. APT blanks were cut from the ingots and electropolished via conventional methods[16]. Annular milling was performed via plasma focused ion beam (PFIB) to position the interfaces near the tip apex. BSE images of the tips were taken for APT data reconstruction. Atom probe data was collected in a CAMECA Invizo 6000 with a detector efficiency of 62%, at 50 K, and dual beam lasers at 200 kHz and 400 pJ. The detection rate was 5%. 3D data reconstruction was accomplished using the software AP Suite 6.3. 1D chemical profiles were extracted from $20\times20\times50$–150 nm^3 cylinders positioned across interphase boundaries. TiB proximity histograms have lengths between 8 and 20 nm and a step size of 0.2 nm. The composition of each phase was determined based on the isosurface objects that encompass the given phase. For phases not enveloped by an isosurface, at least five cubes of varying sizes were placed within the phase, and the composition within these cubes was regarded as the composition of the selected phase.

Results

Figure 1 presents low and high-magnification BSE images. B_4C_0 in Fig. 1(a, b, c) exhibits a 39 ± 3% area fraction of Widmanstätten α-phase embedded in the β matrix, with coarser α-phase along grain boundaries. The addition of B_4C results in the formation of TiB and TiC at a 4:1 ratio through an in-situ reaction during melting, as shown in Fig. 1(d-l). The mechanisms of TiB and TiC formation during solidification, their volume fractions, and the associated mechanical properties have been discussed in previous work[11]. For example, the combined volume fractions of TiB and TiC in B_4C_0.5, B_4C_1.5, and B_4C_3 are approximately 5%, 10%, and 20%, respectively. However, the primary phenomenon of interest here is the refinement and decrease of α-phase with increased volume fractions of TiB and TiC, and subsequent β-phase stabilization. The α-phase in B_4C_0.5 and B_4C_1.5 is significantly finer compared to the α-phase in B_4C_0, with a reduction in area fraction of α-phase observed at 29 ± 3% in B_4C_0.5 and 25 ± 4% in B_4C_1.5. There appears to be a threshold in the fraction of reinforcement particles that drastically reduces α-phase to an almost negligible fraction in B_4C_3 (Fig. 1(k, l)). In this condition, fine α-phase seems to precipitate only from a few TiB particles, as indicated by the yellow arrows.

APT reconstructions of the materials are shown in Figs. 2, 3, 4 and 5. Atom maps are presented in Figs. 2a, 3, 4 and 5a, 3D reconstructions in Figs. 2b, 3, 4 and 5b, the 1D concentration profiles across interphase boundaries in Figs. 2c, 3, 4 and 5c, and proximity histograms in Figs. 3d, 4 and 5d, respectively. In B_4C_0 (Fig. 2), only α- and β-phases are present. Al and O, found as the complex TiO ion here[17] are well-known α-stabilizing elements[18]. β-stabilizing elements Mo and Nb, are identified in the β-phase[7]. Si segregation is observed at the α/β interphase boundary[13].

Figures 3, 4 and 5 show regions containing α, β, and TiB. Figure 6 shows the chemical composition variation for all phases across the samples, it can be seen that there is a slight reduction in Ti in α- and β-phases after additions of B_4C, from a maximum of 88.7 at% in α-phase and 86.5 at% in β-phase in B_4C_0 to 86.8 at% in α-phase and 83.1 at% in β-phase in B_4C_3. Additionally, α-phase becomes enriched in TiO by 1.7 at% and β-phase in Mo by 1.6 at%. Low concentrations of C and B are found in these phases. TiB is slightly off-stoichiometry with 40 at% of B and low concentrations of Mo and Nb. Si and P segregate to the α/TiB interface[13]. In B_4C_1.5 (Fig. 4), the concentration of Ti in α-phase is lower than B_4C_0.5, while Al and TiO are higher. The concentration of TiO is twice as high when compared to B_4C_0. The composition of TiB remains stable in B_4C_0.5 and B_4C_1.5, with slightly higher concentrations of minor elements compared to TiB in B_4C_0.5.

In B_4C_3 (Fig. 5), a 5.3% volume fraction of thin plates of α-phase is identified. This α-phase fraction, however, is likely lower in the bulk of the material, away from the TiB particles (Fig. 1l). The trend of reduction of Ti in α- and β-phase with the increase in B_4C additions is confirmed. α- and β-phases in B_4C_3 have 2.1 at% and 3.4 at% less Ti than B_4C_0, respectively. This changes the Mo equivalent that determines the stability of β-phase according to the contents of β-stabilizing elements[19]. In addition, β-phase becomes enriched in α-stabilizing elements, such as Al and TiO, with double the concentration of the latter (1.6 at%) in comparison to β-phase in B_4C_1.5. On the other hand, α-phase shows the highest enrichment in Mo or roughly three times more than in B_4C_0. Notably, TiB also has a distinct chemical profile, with only 10 at% B and much higher concentrations of Ti, Al, Mo, and TiO than in B_4C_0.5 and B_4C_1.5.

Discussion

The role of TiO deserves comment, as all samples were oxidized during preparation. Despite having better oxidation resistance than commercially pure Ti, Beta 21 S is known to heavily oxidize between 600 and 800 °C[20,21]. TiO ions correlate to the O content and are detected as an effect of laser pulsing during APT, which

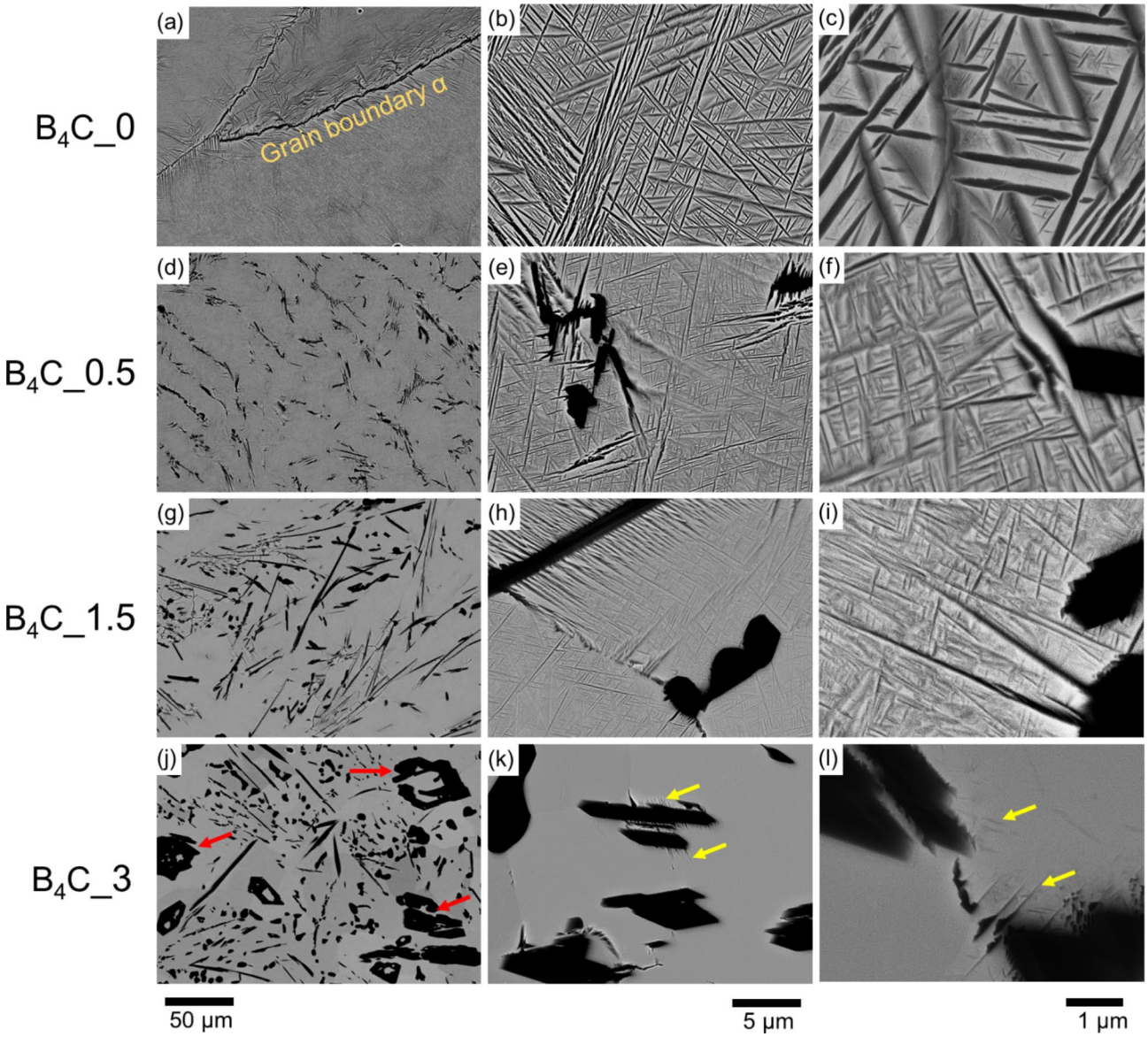

Fig. 1. BSE images of Beta 21 S without B_4C are shown in (**a**–**c**), while Beta 21 S with additions of B_4C are depicted in (**d**–**f**) for B_4C_0.5, (**g**–**i**) for B_4C_1.5, and (**j**–**l**) for B_4C_3. Figures (**c**, **f**, **i**, and **l**) illustrate a refinement and reduction in α-phase with an increase in the volume fraction of TiB and TiC (dark phases). Primary TiB particles are only observed in B_4C_3 (indicated by red arrows), and fine α-phase around eutectic TiB particles are indicated by yellow arrows.

causes thermally assisted evaporation of multiple elements as complex ions[22]. There are several potential sources of oxidation during sample preparation: Raw materials may have not been sufficiently pure, O might be present in the melting chamber, and APT tip preparation via electropolishing may have caused some degree of oxidation. More TiO is observed closer to the apex of the tips (TiO atom maps in Figs. 2, 3, 4 and 5), indicating that PFIB preparation may also contribute to this phenomenon. However, the fact that TiO tends to segregate to α-phase indicates that the most likely source is from the heat treatment, despite being performed in Ar atmosphere[7]. O was adsorbed and enriched into the α-phase during the phase transformation below β-transus.

The formation of TiB makes the materials more susceptible to oxidation, as shown by the increase in TiO in α-phase from B_4C_0 to B_4C_1.5, and in β-phase from B_4C_0 to B_4C_3. Nevertheless, the application of Beta 21 S is generally limited to service temperatures up to 425 °C, minimizing possible oxidation[7]. Maximum TiO retention in α-phase is observed in B_4C_1.5, while α-phase refinement in B_4C_3 results in a decreased TiO concentration. The smaller size and lower volume fraction of α-phase reduce the surface area and diffusion opportunities for O. Additionally, β-phase and TiB are enriched in TiO in B_4C_3, further reducing the O availability for α-phase. While the maximum solubility of O in α is as high as 34 at%[23], there is no consensus on the amount of O that can be in solution in β-phase, with reports indicating concentrations between 4 and 15 at%[24–26]. The proximity histogram in Fig. 5c shows that in the vicinity of TiB, the TiO concentration is as high as 30 at%. This complex

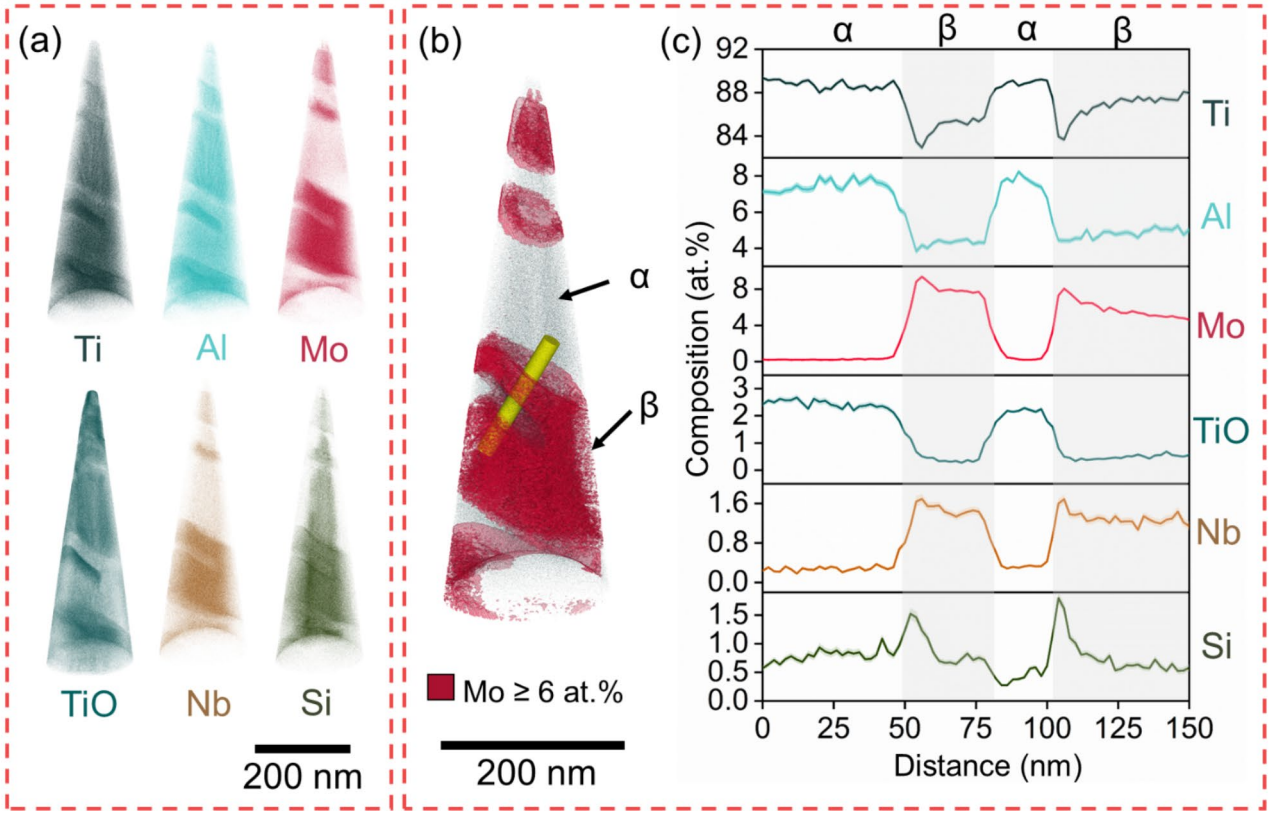

Fig. 2. APT of B_4C_0 showing α-phase and β-phase. (**a**) Atom maps, (**b**) APT reconstruction with isosurfaces highlighting β-phase (red), (**c**) 1D concentration plots and deviation (shaded) across the yellow cylinder.

chemical profile near TiB has a 3-nm area low in Ti, and an increase in Al and Mo at the interface (Fig. 5c). This region contains alternating enrichment and depletion zones, with layers of α- and β-phase not delineated by the isosurfaces used here. The enrichment of Al and TiO in TiB in B_4C_3 corroborates the observation in Fig. 1l, as the removal of α-stabilizing elements from the matrix makes these particles heterogeneous nucleation sites for fine α. Furthermore, O does not seem to negatively affect the mechanical properties of B_4C_3, which has been shown to retain ductility with a maximum compressive strain of 20.5%, and yield strength of 1205 MPa[10]. Similar findings were observed in the recent pioneering development of strong and ductile Ti–O–Fe alloys via additive manufacturing by Song et al.[26], highlighting the importance of understanding the effects of O content in Ti alloys.

The low concentration of B in TiB in B_4C_3 also deserves discussion. The hypereutectic character of C and B in Ti in B_4C_3 explains this phenomenon. As detailed in[11], B_4C_0.5 and B_4C_1.5 are hypoeutectic and near-eutectic, respectively, thus all TiB particles are close to their stoichiometric compositions. In B_4C_3, B was consumed during the formation of primary TiB during solidification (indicated by red arrows in Fig. 1j), and consequently, less B was available for the formation of the remaining eutectic TiB. Therefore, the selected TiB particle in B_4C_3 (Fig. 5) is eutectic. These assumptions are based on Ti-B, Ti-C, and Ti-B_4C phase diagrams available in the literature, thus, the influence of the other alloying elements, particularly Mo, was not considered[27–29]. However, negligible enrichments in Mo and Al are expected in primary TiB, as they formed first from the liquid, as confirmed by thermal analysis[11]. In addition, most of the fine α-phase in B_4C_3 seems to form around small TiB (Fig. 1k), thus, coarse TiB do not contain sufficient α-stabilizing elements to induce heterogeneous nucleation of α-phase. On the other hand, eutectic TiB particles become nucleation sites for α[30,31] as α-stabilizing substitute Ti and B atoms in the orthorhombic crystal structure of TiB. A similar mechanism has been observed in the Ti-5Mo-5 V-8Cr-3Al alloy[32] and in a metal matrix composite steel with TiB_2[33].

The Mo equivalent of Beta 21 S is ~13, thus, 100% of metastable β is retained upon quenching from temperatures above the β transus[7]. Stable β-Ti alloys require a Mo equivalent of >50, as exemplified by the heavily stabilized Alloy C (Ti-35 V-15Cr, wt%) with a Mo equivalent of 47.5, which was still not stable[7]. B_4C_3 is not categorized as β stable due to the presence of fine α-phase, however, the degree of β stabilization is close to Ti-alloys with much higher Mo equivalents. Despite a 26% increase in Mo in β-phase from B_4C_0 to B_4C_3 and corresponding increases of the β-phase stability, a concomitant 32% increase in Al and a four-fold increase in TiO reduce β-phase stability. Thus, a different mechanism must be active in addition to the Mo equivalent in determining the stability of β-phase in this condition.

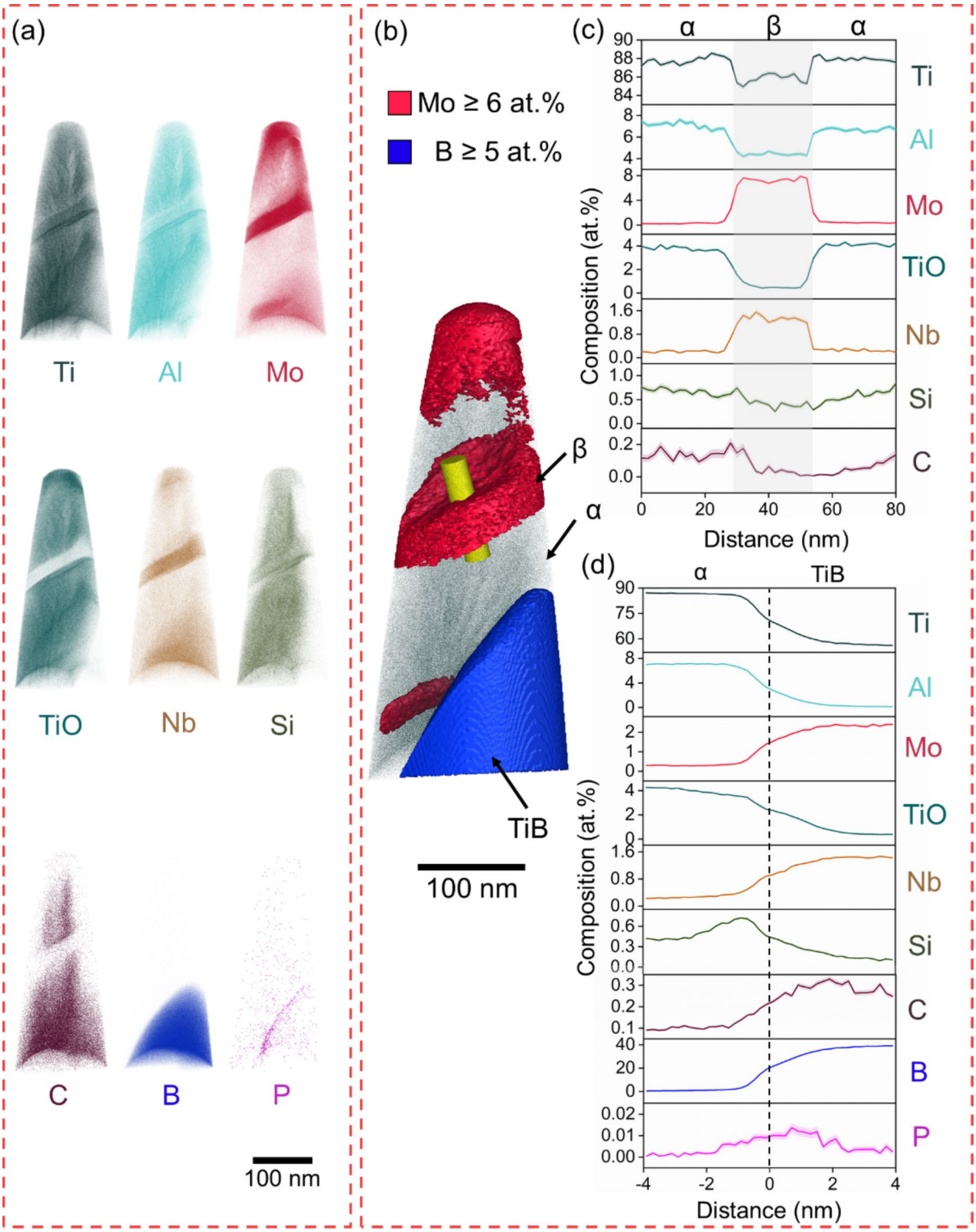

Fig. 3. APT of B_4C_0.5 showing α-phase, β-phase and TiB. (**a**) Atom maps, (**b**) APT reconstruction with isosurfaces highlighting β (red) and TiB (blue), (**c**) 1D concentration plots and deviation (shaded) across the yellow cylinder, and (**d**) α-TiB proximity histogram.

Based on our high-volume APT data, we propose that the enrichment of Mo in α-phase must play a major role in its refinement and β-phase stabilization. Mo, a slow diffusing element, inhibits the growth of α-phase by blocking the influx of Al from β-phase. This is caused by the formation of TiB and TiC, which reduce the availability of Ti and Al in the matrix, as observed by the 20 times higher concentration of Al in the TiB in B_4C_3

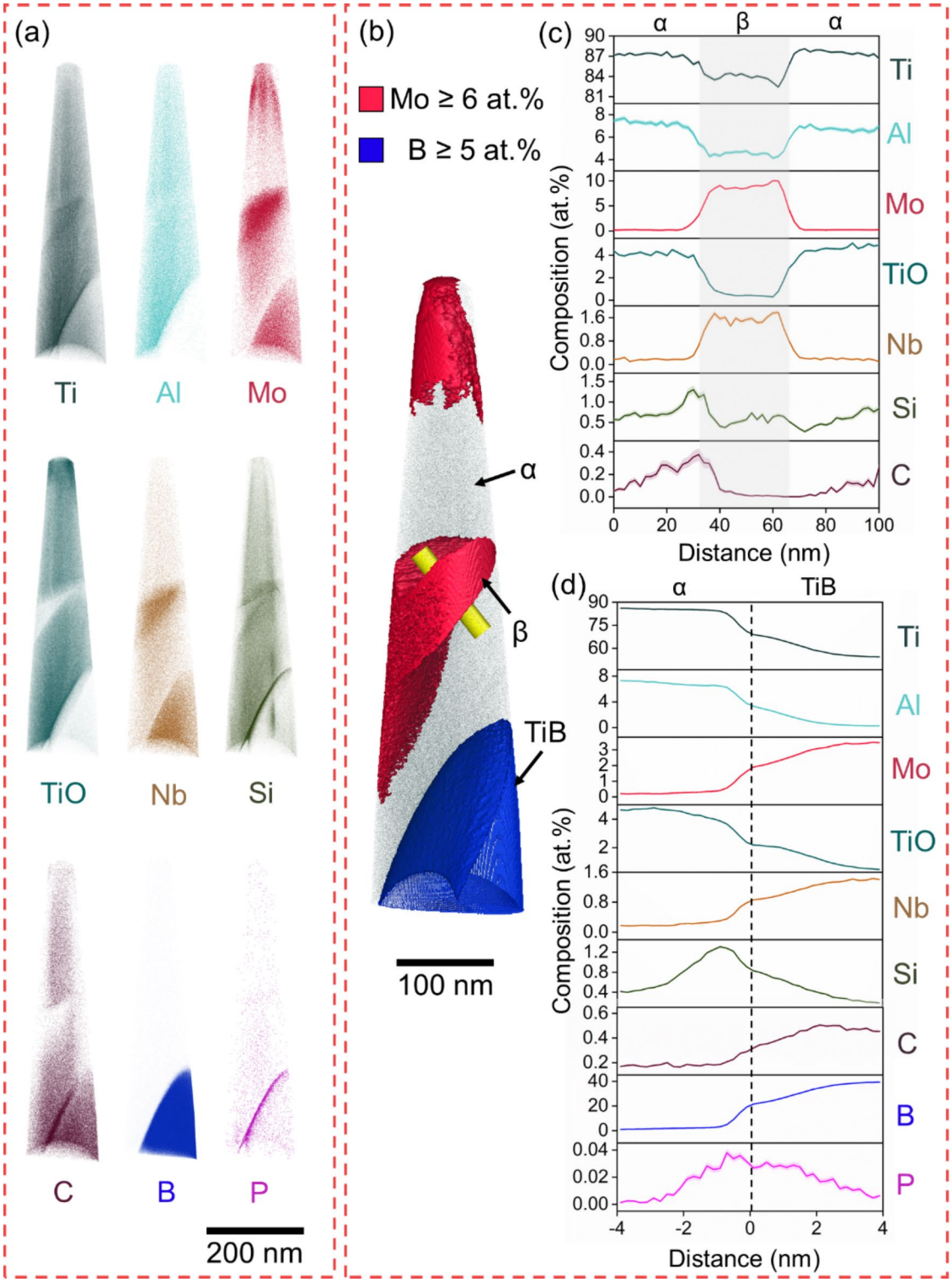

Fig. 4. APT of B_4C_1.5 showing α-phase, β-phase and TiB. (**a**) Atom maps, (**b**) APT reconstruction with isosurfaces highlighting β (red) and TiB (blue), (**c**) 1D concentration plots and deviation (shaded) across the yellow cylinder, and (**d**) α-TiB proximity histogram.

(4 at%) than in B_4C_1.5 (0.2 at%). Interestingly, Nb concentration remains unchanged in all phases, highlighting that the major effect on the increase in β stability must be due to Al and Mo diffusion phenomena.

Lastly, while APT provides exceptional resolution at the sub-nanometre scale[34], it's important to consider its inherent limitations. The technical challenges associated with APT are numerous and well-documented in the literature[16,35,36], but a comprehensive discussion of these issues is beyond this study's scope. However, it's worth

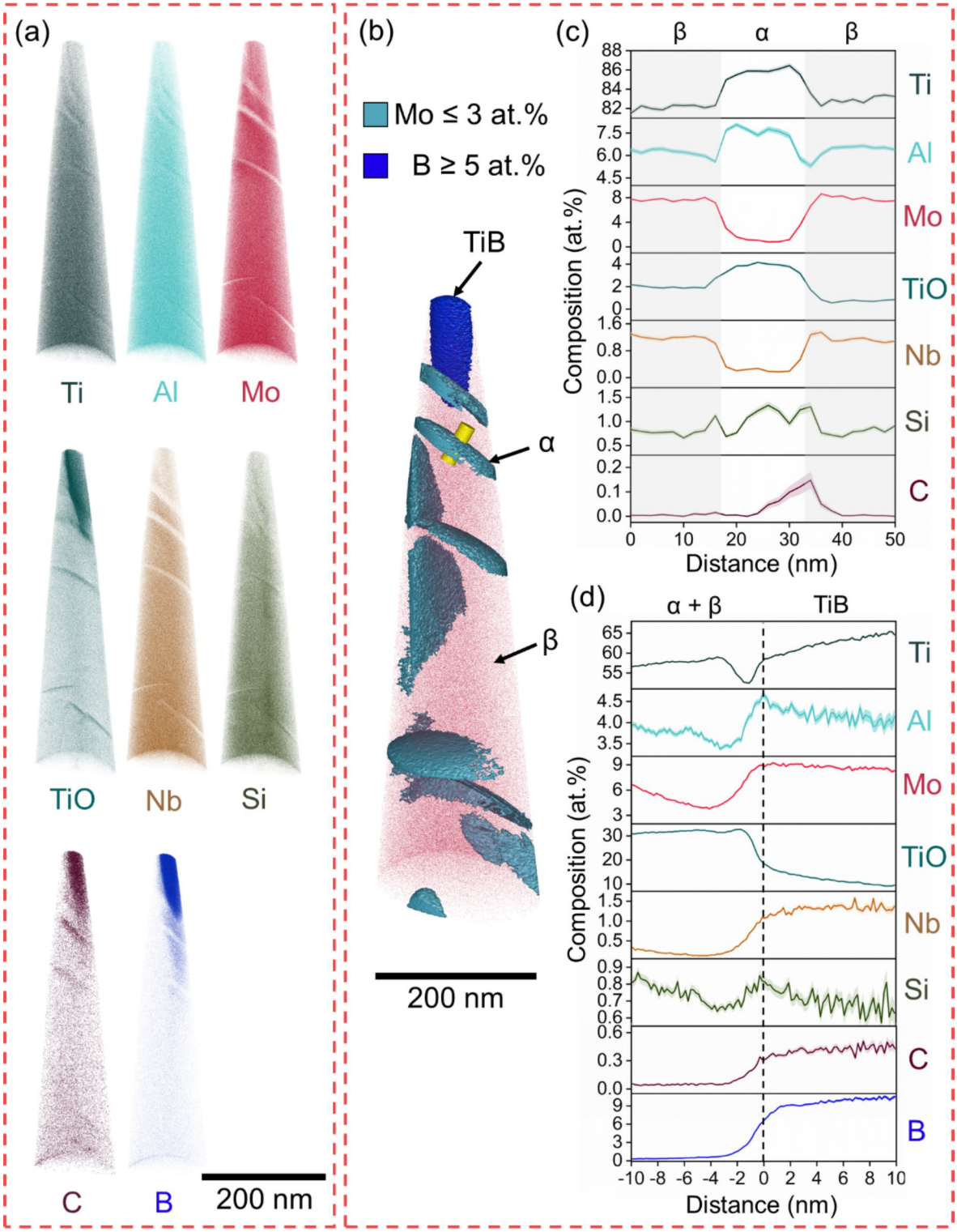

Fig. 5. APT of B_4C_3 showing α-phase, β-phase and TiB. (**a**) Atom maps, (**b**) APT reconstruction with isosurfaces highlighting α (turquoise) and TiB (blue), (**c**) 1D concentration plots and deviation (shaded) across the yellow cylinder, and (**d**) (α + β)-TiB proximity histogram. Refinement of α-phase is observed, which becomes plate-shaped particles.

noting some key artifacts: Local magnification effects can artificially expand segregation zones, particularly those aligned with the tip apex. Non-uniform evaporation due to density variations, such as those caused by borides can lead to inaccurate ion reconstruction at phase boundaries. Currently, fully eliminating or correcting for these artifacts is not possible. Nevertheless, understanding these limitations is crucial for accurate interpretation

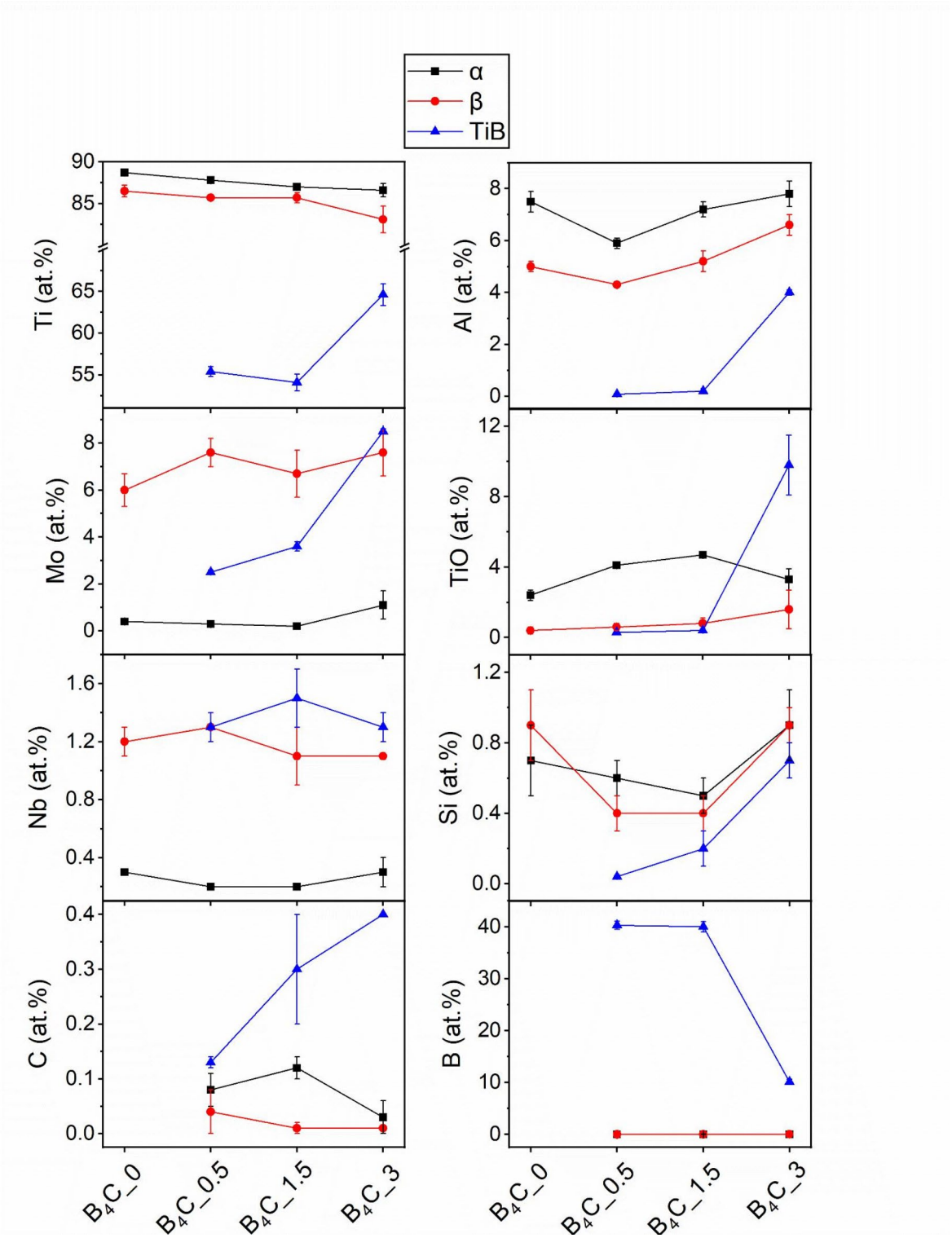

Fig. 6. Chemical composition (at%) of various phases detected by APT in Figs. 2, 3, 4 and 5.

of APT data and readers should keep these factors in mind when analysing and drawing conclusions from the current APT results. We recommend future research to explore additional high resolution techniques to complement these findings.

Conclusions

In summary, furnace cooled β-Ti alloy Beta 21 S with 39% area fraction of α-Ti is refined by adding B_4C followed by the formation of reinforcement particles. The composite material with additions of 0.5 (B_4C_0.5),

1.5 (B_4C_1.5) and 3 wt% (B_4C_3) of B_4C reduce α-Ti to 29%, 25% and 5% fractions, respectively. The β-phase stabilization mechanisms associated with the phase transformations are elucidated via APT. Segregation of Si and P are observed in α/TiB boundaries. Higher TiO formation in α- and β-phase with additions of B_4C may be beneficial to the mechanical strength-ductility relationship, as shown in previous studies[10,26]. In B_4C_3, eutectic TiB particles with low concentrations of B become enriched in Al, and provide nucleation sites for fine α-phase, driving its refinement/decrease. Coarse primary TiB do not seem to promote α-phase formation. Refined α-phase becomes enriched in Mo, inhibiting Al influx, and subsequent α coarsening, promoting a near stable β-phase. Control of α-phase formation via the B_4C additions can lead to stronger β-Ti alloys and composites for applications in next-generation aeroengines.

Data availability

The data that support the findings of this study are available from the corresponding author upon reasonable request.

Received: 15 July 2024; Accepted: 11 October 2024
Published online: 21 October 2024

References

1. Donachie, M. J. *Titanium: A Technical Guide*. (ASM international, 2000).
2. Leyens, C. & Peters, M. *Titanium and Titanium Alloys: Fundamentals and Applications*. (Wiley Online Library, 2006).
3. Hayat, M. D., Singh, H., He, Z. & Cao, P. Titanium metal matrix composites: An overview. *Compos. Part. Appl. Sci. Manuf.* **121**, 418–438 (2019).
4. Boyer, R. R. & Briggs, R. D. The use of β titanium alloys in the aerospace industry. *J. Mater. Eng. Perform.* **14**, 681–685 (2005).
5. Cotton, J. D. et al. State of the art in beta titanium alloys for airframe applications. *JOM*. **67**, 1281–1303 (2015).
6. Ankem, S. & Greene, C. A. Recent developments in microstructure/property relationships of beta titanium alloys. *Mater. Sci. Eng. A*. **263**, 127–131 (1999).
7. Bania, P. J. Beta titanium alloys and their role in the titanium industry. *JOM*. **46**, 16–19 (1994).
8. Du, Z. X. et al. Effects of trace TiB and TiC on microstructure and tensile properties of β titanium alloy. *Mater. Sci. Eng. A*. **596**, 71–79 (2014).
9. Rahoma, H. K. S. et al. Effect of (α + β) heat treatment on microstructure and mechanical properties of (TiB + TiC)/Ti–B20 matrix composite. *Mater. Des.* **87**, 488–494 (2015).
10. Rielli, V. V., Amigó-Borrás, V. & Contieri, R. J. Single step heat treatment for the development of beta titanium composites with in-situ TiB and TiC reinforcement. *Mater. Charact.* **163**, (2020).
11. Rielli, V. V., Amigó-Borrás, V. & Contieri, R. J. Microstructural evolution and mechanical properties of in-situ as-cast beta titanium matrix composites. *J. Alloys Compd.* **778**, 186–196 (2019).
12. Wang, J., Guo, X., Qin, J., Zhang, D. & Lu, W. Morphology evolution of α phase in investment cast titanium matrix composites with B4C additions. *J. Mater. Sci.* **50**, 5674–5683 (2015).
13. Sasaki, T. T. et al. Nucleation and growth of α-Ti on TiB precipitates in Ti–15Mo–2.6Nb–3Al–0.2Si–0.12B. *Phil. Mag.* **91**, 850–864 (2011).
14. Chaudhuri, K. & Perepezko, J. H. Microstructural study of the titanium alloy Ti-15Mo-2.7Nb-3Al-0.2Si (TIMETAL 21S). *Metall. Mater. Trans. A*. **25**, 1109–1118 (1994).
15. Vander Voort, G. F. *Metallography, Principles and Practice*. (ASM international, 1999).
16. Gault, B., Moody, M. P., Cairney, J. M. & Ringer, S. P. *Atom Probe Microscopy*, Vol. 160 (Springer Science & Business Media, 2012).
17. Angseryd, J., Liu, F., Andren, H. O., Gerstl, S. S. A. & Thuvander, M. Quantitative APT analysis of Ti(C,N). *Ultramicroscopy*. **111**, 609–614 (2011).
18. Yumak, N. & Aslantas, K. A review on heat treatment efficiency in metastable β titanium alloys: The role of treatment process and parameters. *J. Mater. Res. Technol.* **9**, 15360–15380 (2020).
19. Wang, Q., Dong, C. & Liaw, P. K. Structural stabilities of β-Ti alloys studied using a New Mo Equivalent Derived from [β/(α + β)] phase-boundary slopes. *Metall. Mater. Trans. A*. **46**, 3440–3447 (2015).
20. Wallace, T. A., Clark, R. K. & Wiedemann, K. E. Oxidation characteristics of Beta-21S in air in the temperature range 600 to 800 C. in *World Conference on Titanium* (1992).
21. Ferreira, L. M., Chaia, N., Coelho, G. C. & Nunes, C. A. Oxidation behavior of STA β-21S alloy and variants [Ti-xNb-yMo-5.6Al-0.5Si at%; x + y = 9.5]. *Corros. Sci.* **203**, 110342 (2022).
22. Kirchhofer, R., Teague, M. C. & Gorman, B. P. Thermal effects on mass and spatial resolution during laser pulse atom probe tomography of cerium oxide. *J. Nucl. Mater.* **436**, 23–28 (2013).
23. Rosa, C. J. Oxygen diffusion in alpha and beta titanium in the temperature range of 932° to 1142°C. *Metall. Trans.* **1**, 2517–2522 (1970).
24. Qian, M. & Cold compaction and sintering of titanium and its alloys for near-net-shape or preform fabrication. *Int. J. Powder Metall.* **46**, (2010).
25. Kofstad, P. High-temperature oxidation of titanium. *J. Less Common. Met.* **12**, 449–464 (1967).
26. Song, T. et al. Strong and ductile titanium–oxygen–iron alloys by additive manufacturing. *Nature*. **618**, 63–68 (2023).
27. Bickerdike, R. L., Hughes, G., Seifert, H. J., Lukas, H. L. & Petzow, G. C-Ti (Carbon-Titanium). *J. Phase Equilibria Diffusion*. **19**, 89–89 (2014).
28. Murray, J. L., Liao, P. K. & Spear, K. E. The B-Ti (Boron-Titanium) system. *Bull. Alloy Phase Diagrams*. **7**, 550–555 (1986).
29. Duschanek, H., Rogl, P. & Lukas, H. L. A critical assessment and thermodynamic calculation of the boron-carbon-titanium (B-C-Ti) ternary system. *J. Phase Equilib.* **16**, 46–60 (1995).
30. An, Q. et al. Insights into in-situ TiB/dual-phase Ti alloy interface and its high load-bearing capacity. *J. Mater. Sci. Technol.* **119**, 156–166 (2022).
31. Hill, D., Banerjee, R., Huber, D., Tiley, J. & Fraser, H. L. Formation of equiaxed alpha in TiB reinforced Ti alloy composites. *Scr. Mater.* **52**, 387–392 (2005).
32. Yang, A. et al. The effect of alloying elements in Ti-5Mo-5V-8Cr-3Al alloy on growth kinetics of TiB whiskers in boride layer. *Mater. Des.* **225**, 111478 (2023).
33. Aparicio-Fernández, R., Springer, H., Szczepaniak, A., Zhang, H. & Raabe, D. In-situ metal matrix composite steels: Effect of alloying and annealing on morphology, structure and mechanical properties of TiB2 particle containing high modulus steels. *Acta Mater.* **107**, 38–48 (2016).
34. Rielli, V. V., Luo, M., Farabi, E., Haghdadi, N. & Primig, S. Interphase boundary segregation in IN738 manufactured via electron-beam powder bed fusion. *Scr. Mater.* **244**, (2024).
35. Gault, B. et al. Spatial resolution in atom probe tomography. *Microsc. Microanal.* **16**, 99–110 (2010).

36. Gault, B. et al. Advances in the reconstruction of atom probe tomography data. *Ultramicroscopy*. **111**, 448–457 (2011).

Acknowledgements
The authors are grateful for the facilities and scientific and technical assistance from the Electron Microscope Unit at UNSW Sydney (Mark Wainwright Centre), Sydney Microscopy & Microanalysis (SMM) at The University of Sydney and FAPESP (2018/21892-0) for support in the TMCs development stage at UNICAMP. Special thanks are extended to Dr. Charlie Kong at UNSW Sydney and Dr. Takanori Sato at the University of Sydney for their valuable technical and scientific support in PFIB and APT, respectively.

Author contributions
V. V. R: Conceptualization, Data curation, Formal analysis, Investigation, Writing - original draft, Writing - review & editing, Project administration. R. J. C.: Resources, Writing - review & editing, Funding acquisition. S. P. : Supervision, Writing - review & editing, Funding acquisition.

Declarations

Competing interests
The authors declare no competing interests.

Additional information
Correspondence and requests for materials should be addressed to V.V.R. or S.P.

Reprints and permissions information is available at www.nature.com/reprints.

Publisher's note Springer Nature remains neutral with regard to jurisdictional claims in published maps and institutional affiliations.